Quantifying the Thermal Stability in Perpendicularly Magnetized Ferromagnetic Nanodisks with Forward Flux Sampling

L. Desplat[1,2,*] and J.-V. Kim[1,†]

[1]*Centre de Nanosciences et de Nanotechnologies, CNRS, Université Paris-Saclay, Palaiseau 91120, France*
[2]*Institut de Physique et Chimie des Matériaux de Strasbourg, CNRS, Université de Strasbourg, Strasbourg 67034, France*

The thermal stability in nanostructured magnetic systems is an important issue for applications in information storage. From a theoretical and simulation perspective, an accurate prediction of thermally activated transitions is a challenging problem because desired retention times are of the order of 10 years, while the characteristic timescale for precessional magnetization dynamics is of the order of nanoseconds. Here, we present a theoretical study of the thermal stability of magnetic elements in the form of perpendicularly magnetized ferromagnetic disks using the forward flux sampling method, which is useful for simulating rare events. We demonstrate how rates of thermally activated switching between the two uniformly magnetized "up" and "down" states, which occurs through domain-wall nucleation and propagation, vary with the interfacial Dzyaloshinskii-Moriya interaction, which affects the energy barrier separating these states. Moreover, we find that the average lifetimes differ by several orders of magnitude from estimates based on the commonly assumed value of 1 GHz for the attempt frequency.

I. INTRODUCTION

The thermal stability of magnetic states is a challenging problem that underpins the utility of magnetism for information storage. It involves understanding the average retention (or dwell) time of a magnetic bit, which typically comprises regions of uniform magnetization in hard disk media, or uniform states in magnetoresistive random-access memories. This retention time, τ, can be obtained as the inverse of the transition rate, $\tau^{-1} = k$, which is governed by an Arrhenius relation of the form [1]

$$k = f_0 e^{-\beta \Delta E}, \tag{1}$$

where f_0 is the Arrhenius prefactor often referred to as the "attempt frequency," ΔE is the energy barrier separating the binary "0" ("up") and "1" ("down") states, $\beta = (k_B T)^{-1}$ is Boltzmann's factor, and T is the temperature.

The vast majority of studies to date have focused on understanding and optimizing the barrier ΔE, whilst assuming a nominal value of $f_0 \simeq 1$ GHz that captures the typical timescales of damped precessional magnetization in strong ferromagnets. Based on this assumption, the typical metric of a 10-year retention time demands that $\Delta = \beta_{300} \Delta E \simeq 50$, in which β_{300} is Boltzmann's factor at

$T = 300$ K, for operation at room temperature—a rule of thumb that has provided guidance both theoretically and experimentally for the feasibility of using various magnetic states for information storage [2–7].

One example of current interest in which the issues of thermal stability are intertwined with the complexity of nonuniform magnetic states concerns ferromagnetic nanostructures with large perpendicular magnetic anisotropy (PMA). Such systems are attractive because they offer larger storage densities than in-plane magnetized systems [8]. However, the reversal process in such systems can be nonuniform [5,7,9–16]. For nanometer-thick ferromagnetic films with lateral dimensions in the tens to hundreds of nanometers, magnetization reversal takes place through the nucleation and propagation of magnetic domain walls, whose energies then govern the energy barrier required to transition from one metastable state to the other [9–11]. Moreover, PMA often involves coupling to strong spin-orbit materials, which can also induce an antisymmetric exchange in the form of a Dzyaloshinskii-Moriya interaction (DMI) [17,18]. Indeed, the presence of DMI has been shown to be detrimental to the thermal stability in such structures [5,7,12], which results from the fact that the DMI reduces the domain-wall energy [19] and therefore the energy barrier.

Recent studies on magnetic skyrmions, however, have shown that the barrier alone does not govern their thermal stability [20–25]. It has been found that a strong entropic

_____

*louise.desplat@ipcms.unistra.fr
†joo-von.kim@c2n.upsaclay.fr

contribution to the prefactor can arise as a result of the complex topology of the energy surface resulting from the large number of degrees of freedom. This can be understood from a generalization of Kramers' transition rate theory [1,26] to a multidimensional phase space, as developed by Langer [27], in which the activation entropy is given by the spectrum of small fluctuations about the initial (meta)stable state and the transition state.

Since the DMI also has a strong influence on the spin wave spectrum in the nominally uniformly magnetized [28] and domain-wall states [29,30], the degree to which entropic contributions influence the thermal stability of PMA memory elements with domain-wall-mediated reversal remains to be explored.

Here, we revisit the question of thermal stability in PMA disks using the method of forward flux sampling (FFS) [25,31–36]. This method was developed for tackling the problem of rare events, which are unlikely to appear during the course of a conventional simulation run, due to the fact that the mean waiting time between events is much larger than the timescale of the dynamics. In magnetism, FFS has been applied to a similar problem of thermal stability in graded media, where its efficacy with respect to brute-force Langevin simulations was clearly demonstrated, and a stability of up to 1417 years was computed [35]. The method has also recently been applied to the study of skyrmion lifetimes, where agreement was found with another approach based on Langer's theory [25].

The remainder of the article is organized as follows. In Sec. II, we present the system studied and the implementation of the forward flux sampling method. In Sec. III, we discuss the application of the method to determine the change in average dwell time with the Dzyaloshinskii-Moriya interaction. A discussion and concluding remarks are given in Sec. IV.

II. GEOMETRY AND METHOD

The system studied comprises a perpendicularly magnetized ferromagnetic disk, which simulates the free magnetic layer in a magnetic memory device. Following Ref. [5], we consider a Co-Fe-B film with a saturation magnetization of $M_s = 1.03$ MA/m, an exchange constant of $\mathcal{A} = 10$ pJ/m, and a perpendicular anisotropy constant of $K_u = 0.77$ MJ/m^3. We also take into account the presence of an interfacial Dzyaloshinskii-Moriya interaction, D, whose strength is varied. We model a 1-nm-thick disk with a diameter of 32 nm, which is discretized with finite difference cells $1 \times 1 \times 1$ nm^3 in size. Note that the grid size does not affect the upcoming results as long as the lateral dimension of the unit cell is smaller than the characteristic domain-wall width, $\delta = \sqrt{\mathcal{A}/K}$. Using the uniaxial anisotropy constant K_u yields $\delta = 3.6$ nm. With the effective anisotropy treatment that is used in Secs. III C and III D, $K_{\text{eff}} = 187$ kJ/m^3 [5], and the wall

width becomes $\delta = 7.3$ nm. Last, let z denote the axis perpendicular to the film, which lies in the x-y plane.

We use the micromagnetic approximation and consider the Langevin dynamics of the magnetization vector, $\mathbf{m}(\mathbf{r},t) \equiv \mathbf{M}(\mathbf{r},t)/M_s$, such that $\|\mathbf{m}(\mathbf{r},t)\| = 1$. The energy density functional reads

$$\varepsilon = \mathcal{A}(\nabla\mathbf{m})^2 - Km_z^2 + D(L_{zx}^{(x)} + L_{zy}^{(y)}) + \varepsilon_d, \quad (2)$$

in which the

$$L_{ij}^{(k)} = m_i \frac{\partial m_j}{\partial x_k} - m_j \frac{\partial m_i}{\partial x_k} \quad (3)$$

are Lifshitz invariants [37], ε_d is the dipole-dipole interaction (DDI) as implemented in MuMax3 [38], and

$$K = \begin{cases} K_{\text{eff}} & \text{if } \varepsilon_d = 0, \\ K_u & \text{otherwise.} \end{cases} \quad (4)$$

The total micromagnetic energy of the system thus reads,

$$E = \int_{\text{system}} \varepsilon \, dV. \quad (5)$$

The Langevin dynamics is obtained by stochastic time integration of the Landau-Lifshitz-Gilbert equation with a fluctuating thermal field [39],

$$\frac{d\mathbf{m}}{dt} = -\gamma_0 \mathbf{m} \times (\mathbf{H}_{\text{eff}} + \mathbf{h}_{\text{th}}) + \alpha\mathbf{m} \times \frac{d\mathbf{m}}{dt}, \quad (6)$$

where $\gamma_0 = \mu_0\gamma$, in which γ is the gyromagnetic constant, and α is the Gilbert damping constant. The dynamics is governed by the deterministic effective field $\mathbf{H}_{\text{eff}} = -(\mu_0 M_s)^{-1}\delta E/\delta\mathbf{m}$, which is obtained from the variational derivative of the total micromagnetic energy E [Eq. (5)] with respect to the magnetization, and a stochastic field $\mathbf{h}_{\text{th}}$ that takes into account finite temperature effects. This thermal field has zero mean, $\langle\mathbf{h}_{\text{th}}\rangle = 0$, and represents a Gaussian white noise with the spectral properties

$$\langle h_{\text{th},i}(\mathbf{r},t)h_{\text{th},j}(\mathbf{r}',t')\rangle = \frac{2\alpha k_B T}{\mu_0 V}\delta_{ij}\delta(\mathbf{r}-\mathbf{r}')\delta(t-t'), \quad (7)$$

where i,j represent the different Cartesian components of the field vector, and V is the volume of the unit cell. We use two methods to compute this stochastic time integration: a homemade code that employs a stochastic Heun scheme [23,25,40], and the MuMax3 code [38] with an adaptive timestep scheme [41].

Let A denote the initial magnetic state, which corresponds to the uniformly magnetized state along the $+z$ direction, and let B denote the second degenerate metastable state, which is uniformly magnetized along $-z$

and separated from A by an energy barrier, ΔE. Our goal is to compute the average lifetime τ of state A at finite temperature.

Estimating τ directly through brute-force Langevin dynamics simulations would involve starting with A as the initial configuration and integrating Eq. (6) until state B is reached. This process would then require being repeated a few hundred times to obtain reasonable statistics. Because of the precessional dynamics, typical timesteps for the numerical time integration are in the range of 1 to 100 fs, so it does not appear fruitful to proceed with this program of work while τ is of the order of years for technologically relevant systems.

If the transition between the two time-invariant steady states A and B is fast compared to the mean waiting time between transitions, $\tau = k_{AB}^{-1}$, then k_{AB} is also time invariant, and the FFS method [31–34] can be used instead of the brute-force method to estimate the rate constant of such rare events [25,35,36]. The basic idea of the FFS approach is illustrated in Fig. 1.The method involves generating trajectories of the system between A and B in a ratchetlike manner. This is achieved through a series of

(a)

A B

$\zeta = \langle m_z(\mathbf{r}) \rangle$

(b)

A B

λ_A λ_0 λ_1 λ_i λ_{n-1} $\lambda_n = \lambda_B$

(c)

A B

λ_A λ_0 λ_1 λ_i λ_{n-1} $\lambda_n = \lambda_B$
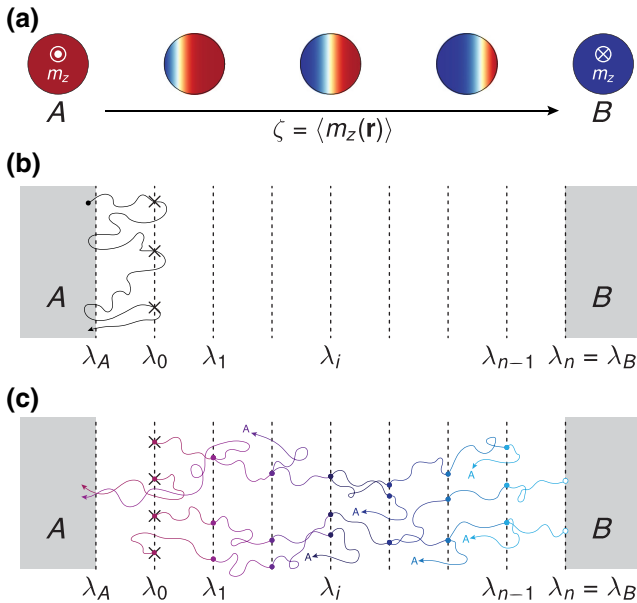
FIG. 1. Schematic of the forward flux sampling method. (a) Minimum energy path for magnetization reversal between the up and down states through domain-wall nucleation and propagation. Progression along the reaction coordinate is parameterized by the order parameter ζ. (b) Sequence of interfaces $\{\lambda\}$ separating basins A and B. We record N_0 crossings at the interface λ_0 when the system starts in A and successfully reaches λ_0. (c) Simulated trajectories between subsequent interfaces. The micromagnetic configuration is stored at λ_{i+1} for each successful crossing from λ_i to λ_{i+1}, which serves as a starting point for Langevin dynamics simulations toward the next interface. Failed crossings involve returns to basin A.

noninteresecting interfaces, $\{\lambda_A, \lambda_0, \lambda_1, \ldots, \lambda_{n-1}, \lambda_n = \lambda_B\}$, in phase space. These are defined as isosurfaces of a monotonically varying order parameter, ζ, as $\lambda(\zeta)$. For the problem studied here, the order parameter is chosen to be the spatial average of the m_z component of the magnetization, $\zeta \equiv \langle m_z(\mathbf{r}) \rangle = (V)^{-1} \int dV \, m_z(\mathbf{r})$, and decreases monotonically between A and B. The A basin is thus defined for $\zeta > \zeta_A$. Similarly, the B basin is defined for $\zeta < \zeta_B$. A choice of order parameter that is close to the reaction coordinate—i.e., the minimum energy path (MEP) of highest statistical weight through phase space—improves the computational efficiency of the method. All trajectories from A to B must traverse each interface at least once.

The overall transition rate is expressed as

$$k_{AB} = \Phi_{A,0} P_B, \qquad (8)$$

where $\Phi_{A,0}$ represents the flux of trajectories from A to the first interface λ_0, and $P_B \equiv P(\lambda_B \mid \lambda_0)$ is the probability that a trajectory that crossed λ_0 coming from A reaches λ_B before returning to basin A. The quantity $\Phi_{A,0}$ can be obtained in a straightforward manner since the trajectories emanating from A cross the λ_0 interface with high frequency as a result of its proximity. On the other hand, the probability P_B will typically be very small for rare events. However, calculating this probability becomes manageable by decomposing it into a product of partial fluxes at each interface,

$$P_B \equiv P(\lambda_n \mid \lambda_0) = \prod_{i=0}^{n-1} P(\lambda_{i+1} \mid \lambda_i), \qquad (9)$$

where the conditional probability $P(\lambda_{i+1} \mid \lambda_i)$ represents the probability that a trajectory starting at λ_i reaches λ_{i+1} before returning to basin A.

Computation of the rate k_{AB} proceeds in two steps. The first involves initializing the system in A and performing a Langevin dynamics simulation by stochastic time integration of Eq. (6). This simulation is used to collect micromagnetic configurations at λ_0 that result from instances in which the system commences in A and crosses the interface λ_0, as shown in Fig. 1(b). One then waits for the system to return to A before the next crossing configuration at λ_0 can be saved. The simulation proceeds until N_0 such configurations have been obtained, at which the flux of trajectories out of A that cross λ_0 can be estimated as $\Phi_{A,0} = N_0 / \Delta t_{\text{sim}}$, where Δt_{sim} is the total simulated time required to obtain the N_0 crossings. Note that Δt_{sim} should not include the time the system may have spent in the B basin. The second step involves computing the probability P_B and is illustrated in Fig. 1(c). It begins by selecting at random a stored configuration at λ_0 and performing a Langevin dynamics simulation until either the system returns to A, which counts as a failed crossing, or it reaches

the next interface λ_1, in which case the micromagnetic configuration at λ_1 is stored. This process is repeated M_0 times, and the probability of reaching λ_1 from λ_0 is computed as $P(\lambda_1 \mid \lambda_0) = N_0^s / M_0$, where N_0^s denotes the number of successful crossings of λ_1. The procedure then continues in an analogous manner for the subsequent interfaces until λ_B is reached, as shown in Fig. 1(c). The overall FFS simulation is successful if at least one trajectory reached λ_B.

III. VARIATION OF THERMAL STABILITY WITH DMI

A. Interface definition

The interfaces used to compute the rate of magnetization reversal in the nanodisk are constructed as follows. The boundary of the A basin, λ_A, is determined by the median of the value of $m_{z,0} = \langle m_z \rangle$ of the thermally equilibrated state, which leads to A being defined as $\zeta > m_{z,0}$. By symmetry, we define λ_B at $\zeta_B = -m_{z,0}$, with B occupying the region of phase space $\zeta < -m_{z,0}$. We note that $m_{z,0}$ is a temperature-dependent quantity and also varies strongly as a function of the DMI, since the boundary conditions at the disk edges result in a canting of the magnetic moments away from the z axis [28,42]. Instead of spacing the interfaces equally from $\zeta = m_{z,0}$ to $\zeta = -m_{z,0}$, we choose instead a weighting function based on the $\tanh(\zeta)$ function that better mimics the reversal path. For example, for a magnetization profile of the form $\langle m_z \rangle(\chi) = \tanh(\chi)$, where χ is the reaction coordinate [43], the choice of interface would represent regular spacing along the χ axis, rather than $\langle m_z \rangle$. Ultimately, this is a matter of convenience, as the FFS method is not overly reliant on the particular placement of interfaces, which should in principle only affect the efficiency of the method [33], as we show further below.

B. Underdamped limit with full dipolar interactions

We first present results using the MuMax3 code with full dipolar interactions, a realistic damping value of $\alpha = 0.01$ [44], a variable DMI constant D between 0 and 2 mJ/m^2, and $T = 300$ K. For this set of simulations, we use $N_0 = 50$ and $M_0 = 1000$ with 16 interfaces ($n = 15$).

In Fig. 2, we present the averaged magnetization configurations at different interfaces for three values of D. The configurations represent the stored state at an interface λ_i following a successful traversal from λ_{i-1}. Since wall nucleation is not restricted to a particular edge of the disk, there is a multitude of paths through which the wall can traverse the disk during the reversal. In order to obtain a meaningful average, we first rotate each configuration such that wall displacement takes place from left to right during the reversal, in line with the schematic presented in Fig. 1(a).
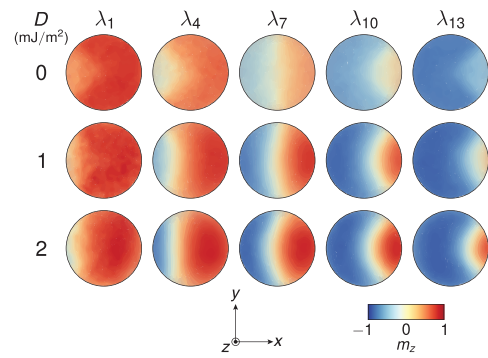

FIG. 2. Averaged magnetization configurations at different interfaces λ for different runs involving three values of the DMI, D. Here λ_7 corresponds to the interface at which $\zeta = 0$. Each configuration is rotated about the disk center such that wall propagation proceeds from left to right during reversal before the averaging procedure is performed. Note that, although we represent the edges of the disk as smooth, in reality, the boundary exhibits a staircase effect due to the discretization.

The overall behavior is similar for all considered values of D, and resembles the minimum energy paths predicted in earlier works from path-finding schemes [5,10,12,43]. This is consistent with the fact that the MEP typically constitutes the path of highest statistical weight, and thus corresponds to the path followed by the system on average. The first interface involves the apparition of a nucleation zone at the disk boundary, which is most pronounced for $D = 2$ mJ/m^2 by virtue of the greater tilt of the magnetization at the disk edges. This proceeds with the propagation of a domain wall that sweeps through the disk. In the presence of DDIs, we observe that the domain wall exhibits a strong curvature at the disk center for large values of the DMI, in contrast to the MEP in which the wall in the center is typically straight [5]. This seems to be a dynamical effect arising from the combined actions of the DMI and the DDI. The direction of the curvature is likely determined by the fact that, in FFS, magnetic configurations are stored for forward trajectories only, i.e., trajectories in which the walls progresses from left to right. Without DDI, we recover an average straight wall configuration in the disk center.

The properties of the conditional probabilities $p_{i-1} \equiv P(\lambda_i \mid \lambda_{i-1})$ are presented in Fig. 3. The variation of p_{i-1} with the order parameter ζ_i is shown in Fig. 3(a). For the first set of interfaces in the vicinity of A, the conditional probabilities lie around 10%, and then progressively increase as the trajectories propagate toward $\lambda_B = \lambda(\zeta_B)$. For $D = 0$ mJ/m^2, there is a sharp increase after $\zeta \simeq 0.4$ (λ_5) and saturation is attained after $\zeta \simeq -0.4$ (λ_{11}). The variation is more gradual for the cases with finite values of D, where, interestingly, for $D = 2$ mJ/m^2, saturation toward unity does not occur. This suggests that numerous recrossings of the barrier take place even when the state approaches the vicinity of B. This is a general feature of all
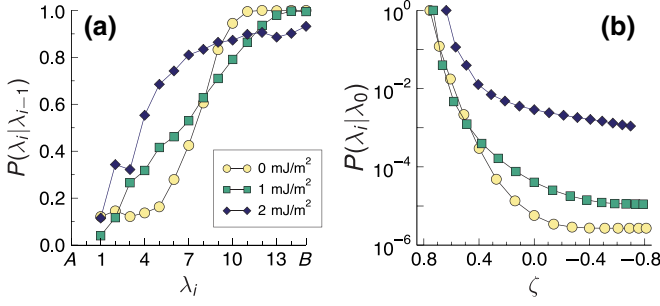
FIG. 3. In the underdamped limit with DDIs: (a) Conditional probabilities $P(\lambda_i \mid \lambda_{i-1})$ as a function of the interface λ_i for three different values of the DMI D. (b) Cumulative conditional probabilities $P(\lambda_i \mid \lambda_0)$, determined from the cumulative products of $P(\lambda_i \mid \lambda_{i-1})$ in (a), as a function of the order parameter ζ for three values of D.

the cases studied, albeit to different degrees, which is evidenced by the fact that p_{i-1} approaches 1 well beyond the interface where $\zeta = 0$, i.e., at the top of the energy barrier. In other words, the underdamped dynamics of the magnetization precession means that reversal is not guaranteed even if the energy barrier is crossed [40].

This can also be seen in the evolution of the cumulative product $P(\lambda_i \mid \lambda_0)$ with ζ, shown in Fig. 3(b), which describes the probability of reaching λ_i given the starting point of λ_0. This function is constructed from the conditional probabilities in Fig. 3(a) as $P(\lambda_i \mid \lambda_0) = \prod_{j=0}^{i-1} P(\lambda_{j+1} \mid \lambda_j)$. In this representation, we observe that most of the evolution in $P(\lambda_i \mid \lambda_0)$ occurs for $\zeta > 0$, i.e., as the energy barrier is surmounted from A, with a further reduction by a factor of approximately 5 occurring due to barrier recrossings for $\zeta < 0$.

C. Overdamped limit with effective perpendicular anisotropy

The data presented in Figs. 2 and 3 represent a single FFS run. While the computational time required to execute this task is considerably shorter than full Langevin dynamics simulations of the entire reversal process, it is not feasible to obtain statistics of the interface probabilities, i.e., different realizations of the sampling for a given value of D, within a reasonable timeframe. For instance, each data point for the conditional probability in Fig. 3(a) required 1 to 3 days of simulation time on a single NVIDIA GTX 1080 graphics processor unit. Part of this difficulty stems from the calculation of the long-range dipolar interactions, which is computationally intensive. Another difficulty involves the underdamped nature of the precessional dynamics, which results in multiple recrossings at any given interface.

To ascertain whether the trends observed in Fig. 3 are representative of the reversal process, we conduct a different set of simulations in which the long-range dipolar
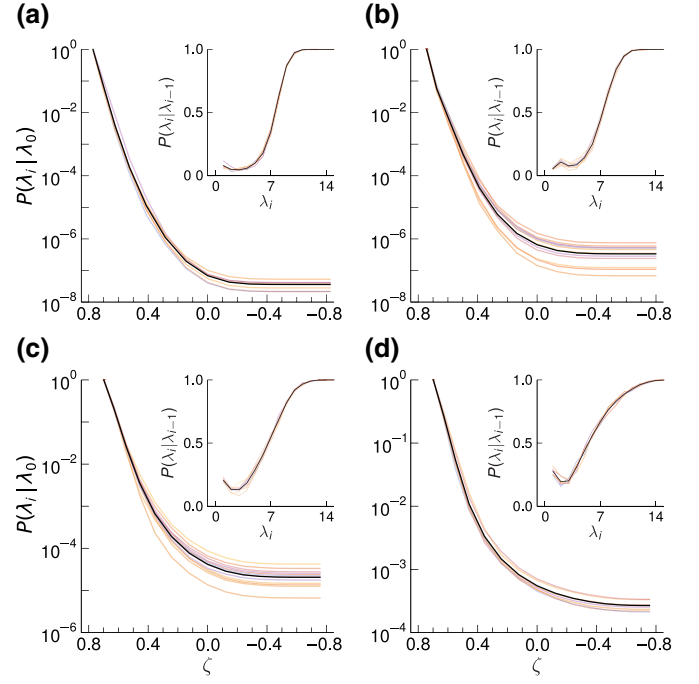

FIG. 4. In the overdamped limit with effective anisotropy, cumulative probability $P(\lambda_i \mid \lambda_0)$ as a function of the order parameter ζ for different values of D: (a) 0.5, (b) 1.0, (c) 1.5, and (d) 2.0 mJ/m². The insets show the conditional probability $P(\lambda_i \mid \lambda_{i-1})$ as a function of the interface λ_i. The colored lines represent single FFS runs, while the solid black lines represent averages over the different runs.

interactions are approximated by a rescaling of the perpendicular anisotropy constant, i.e., $K_{\text{eff}} = K_u - \frac{1}{2}(N_z - N_x)\mu_0 M_s^2 = 187$ kJ/m³ [5], where $N_x = 0.0418$ and $N_z = 0.916$ are demagnetizing factors of the disk [45]. The use of a local approximation for the dipolar interaction is less computationally intense and speeds up the simulation time.

We first consider the overdamped limit, $\alpha = 0.5$, which facilitates comparisons with Langer's theory [43]. The cumulative probability function $P(\lambda_i \mid \lambda_0)$ for different values of the DMI is shown in Fig. 4. The corresponding conditional probabilities, $P(\lambda_i \mid \lambda_{i-1})$, are shown in the inset of each subfigure. For each value of D, the distinct FFS runs performed (between 7 and 12) are represented by the different colored curves, while the ensemble-averaged result is given by the black curve. While there is some spread in the final probability $P(\lambda_B \mid \lambda_0)$, the curves for the cumulative probability and the conditional probability share the same qualitative trend for a given value of D. The manner in which the shape of the $P(\lambda_i \mid \lambda_{i-1})$ curves change as D is increased also mirrors the evolution seen for the case presented in Fig. 3(a), where the S-shaped variation at $D = 0$ transitions to more of a square-root-like behavior at $D = 2$ mJ/m².

D. Underdamped limit with effective perpendicular anisotropy—optimization procedure

1. Optimization

In the underdamped limit of $\alpha = 0.01$, similar to Sec. III B, recrossings are more frequent and the system deviates more significantly from the MEP, resulting in longer waiting times between magnetization reversals compared to the overdamped case. Longer waiting times typically imply longer CPU times. Nevertheless, the FFS simulation times can be reduced through several methods.

First, many trial runs at a given interface can be performed simultaneously on one or multiple CPU units. The only requirement is that the simulation waits for all trials run at one interface to terminate before moving on to the next interface. This can be managed via message passing interface on multiple nodes, or a simple Bash script on a single node.

Second, the parameters of the FFS run can be optimized in order to improve the efficiency of the method, as derived by Borrero and Escobedo [34]. The variance of the rate yielded by the trial runs, i.e., $V[P_B]$ [32], is minimized under the constraint that the total rate k_{AB} must remain constant. The best efficiency for FFS is obtained for a minimal relative variance of the rate, which is yielded by a constant flux of partial trajectories through all interfaces, i.e., $M_i p_i = \text{const}$. We define the relative variance of the rate as [32]

$$\mathcal{V} = \sum_{i=0}^{n-1} \frac{q_i}{p_i k_i}, \tag{10}$$

where we have used the simplified notation $p_i \equiv P(\lambda_{i+1} \mid \lambda_i)$, $q_i \equiv 1 - p_i$, and $k_i \equiv M_i/N_0$. One may therefore either optimize the number of trial runs per interface, $\{M_i\}$, at a fixed interface placement, or optimize the placement of the interfaces, $\{\zeta_i\}$, at fixed $\{M_i\}$. In the latter case, the interface placement is used to optimize the conditional probabilities $\{p_i\}$.

In this work, we choose to set $M_i = M_0$ at all interfaces, and optimize the interface placement. We proceed as follows. First, a full FFS simulation is carried out with $N_0 = 100$ and $n + 1 = 40$ interfaces whose positions in phase space are chosen as described in Sec. III A. Note that, once $\Phi_{A,0}$ in Eq. (8) has been determined, then if an estimate of the final rate k_{AB} is available—for instance, from Langer's theory [25,27,43], or from previous runs with similar parameters—it is then possible to estimate a value of M_0 that yields a low relative variance of the rate $\mathcal{V}$, as defined in Eq. (10). For instance, one may aim for $\mathcal{V} = 1$. For the present set of parameters, we use values of M_0 spanning from 1000 at high D to 2800 at low D. Once the initial run has terminated, the interface placement is optimized to obtain $p_i = p_i^{\text{opt}} = (P_B)^{1/n}$ for all i by following the procedure described in Ref. [34], and illustrated
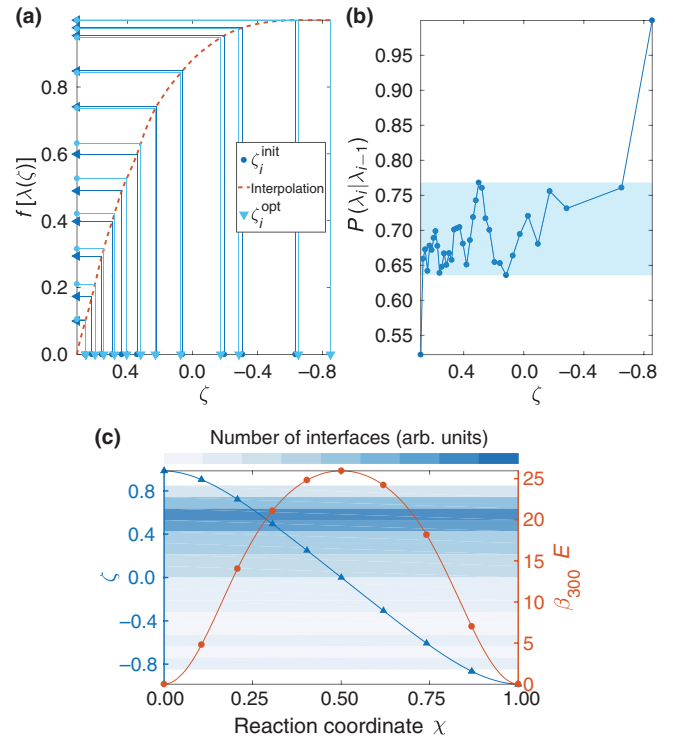

FIG. 5. Example of interface optimization in FFS. (a) The new values of the order parameter $\{\zeta_i^{\text{opt}}\}$ are obtained by inverting the interpolation function in Eq. (11), which is plotted with a dotted line. The $\{\zeta_i^{\text{opt}}\}$ are designed to approach a constant flux of partial trajectories through each interface. (b) Partial fluxes $P(\lambda_i \mid \lambda_{i-1})$ as a function of the order parameter ζ resulting from the interface optimization procedure. With the exception of the first and last interfaces, the values are found within the shaded area. (c) Evolutions of the order parameter ζ (left axis, triangles) and the energy normalized by the thermal energy at 300 K, $\beta_{300}E$ (right axis, circles), as a function of the reaction coordinate χ along the minimum energy path. The interfaces are optimized again after the first FFS run with the interfaces shown in (a). The number of interfaces per interval of ζ is represented by the colored background, where a darker color corresponds to more interfaces. Denser interfaces are needed before the saddle point, around $\zeta = 0.58$.

in Fig. 5. A monotonic interpolation function is needed in order to establish a one-to-one correspondence between the $\{p_i\}$ and the $\{\zeta_i\}$. A possible choice for such a function is

$$f[\lambda(\zeta_i)] = \frac{\sum_{j=0}^{i-1} \ln p_j}{\sum_{j=0}^{n-1} \ln p_j}, \tag{11}$$

which reduces to the optimal values $f(\zeta_i^{\text{opt}}) = i/n$ when $p_i = p_i^{\text{opt}}$. The initial set of $f(\zeta_i^{\text{init}})$ is computed from the $\{\zeta_i^{\text{init}}\}$ according to Eq. (11). The sets of ζ_i^{init} and $f(\zeta_i^{\text{init}})$ are respectively shown as dark blue circles and dark blue triangles in Fig. 5(a) for $D = 1$ mJ/m^2. The resulting dataset is interpolated, which is shown as a red dotted line. One then computes the optimal values, $f(\zeta_i^{\text{opt}})$, as

indicated by pale blue circles. The corresponding values of the order parameter $\{\zeta_i^{\text{opt}}\}$ that determine the placement of the new interfaces are found by inverting the interpolation function, and are shown as pale blue triangles. Note that, for readability, we do not show all the interfaces in Fig. 5(a). In practise, only a single FFS run is typically carried out per value of D, and the computed probabilities are then used to optimize the interfaces for the next value of D, and so on with iteratively decreasing D.

In Fig. 5(b), we show the partial flux through interface i coming from interface $i - 1$, p_{i-1}, as a function of ζ at $D = 0.75$ mJ/m². The interface placement is that obtained from the interface optimization procedure carried out using the results at $D = 1$ mJ/m². Apart from the flux through λ_1 and $\lambda_n = \lambda_B$, we have $0.64 \leq p_{i-1} \leq 0.77$, as shown by the shaded area in Fig. 5(b). For $N_0 = 100$ and $M_0 = 2800$, the relative variance of the rate yielded by the FFS run is $\mathcal{V} = 1.37$ and the computed lifetime of the uniform state at 300 K is $\tau = 0.013 \pm 0.002$ s.

Lastly, in Fig. 5(c) we show the variations of the order parameter ζ and the energy normalized by the thermal energy at $T = 300$ K, $\beta_{300}E$, as a function of the normalized reaction coordinate χ at D = 0.75 mJ/m², as computed by the geodesic nudged elastic band (GNEB) method [46] in Ref. [43]. The reaction coordinate χ goes from 0 in state A, to 0.5 at the barrier top, to 1 in state B. The colored background indicates the number of optimized interfaces per small interval of ζ with arbitrary units, with a darker color corresponding to more interfaces. During the initial FFS run, the non-optimized interfaces are evenly spaced out along the reaction coordinate for $\zeta > 0$, similarly to the images in the GNEB method, which are shown as blue triangles. The optimized interfaces are not evenly spaced out, but are denser about halfway to the saddle point ($\zeta \simeq 0.58$ and $\chi \simeq 0.27$). In terms of the energy profile, this corresponds to the region preceding the barrier top. Denser interfaces enable a better sampling of the rare partial trajectories that progress to the next interface in that region. Once these trajectories have been selected, they are more likely to cross the barrier in the following trial runs, and the subsequent interfaces can be more spaced out.

2. Results

The Langevin simulations in the underdamped regime are performed with a homemade code [23,25] with an effective anisotropy and a single FFS run per value of D. Each run is carried out on a single CPU unit (Intel Xeon Gold 6130 processor), and a maximum of 65 simultaneous trial runs. A complete run at $T = 300$ K and $n + 1 = 40$ interfaces took between about a week for high D ($M_0 = 1000$) and about two weeks for low D ($M_0 = 2800$). Note that the homemade code that is used is not particularly
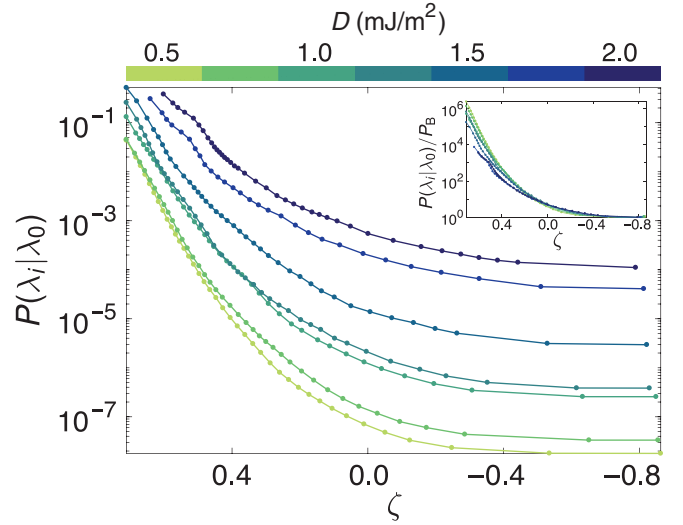

FIG. 6. In the underdamped limit with effective anisotropy, cumulative probability $P(\lambda_i \mid \lambda_0)$ as a function of the order parameter ζ for different values of D. The inset shows the same probabilities normalized by $P_B = P(\lambda_B \mid \lambda_0)$. The normalized probabilities for different values of D are superimposed because the flux of barrier recrossings remains a constant fraction of the rate constant, independently of D.

optimized, and that FFS runs with MuMax3 are typically much faster.

In Fig. 6, we show, for a set of trajectories starting at λ_0, the cumulative probability to reach λ_i, $P(\lambda_i \mid \lambda_0)$, as a function of the order parameter ζ for different values of D. We find that overall the behavior of the system is similar to the overdamped behavior of Sec. III C, with profiles of the cumulative fluxes similar to those shown in Fig. 4. Once more, the cumulative flux of trajectories decreases with decreasing D. The inset in Fig. 6 shows the cumulative fluxes normalized by P_B, i.e., $P(\lambda_i \mid \lambda_0)/P_B$, for all values of D. We find that in this viewpoint the graphs largely overlap. Since the energy profile remains symmetric when D is varied, the rate of recrossing seems to be a somewhat constant fraction of the transition rate, and the DMI does not fundamentally impact the system in that sense.

E. Comparison of lifetimes

The key result of this study is presented in Fig. 7, where the mean lifetime of the A state, τ, is shown as a function of D for the three cases discussed above. For memory elements, it corresponds to the information retention time.

In Fig. 7(a), the results for the simulations with full dipolar interactions are shown. Since these results are obtained from only a single FFS run, we estimate the uncertainty in the lifetime by using the relative variance of the rate $\mathcal{V}$, as defined in Eq. (10). We recall that $M_i = M_0 = 1000$ for all interfaces for this case and $N_0 = 50$. The statistical error in
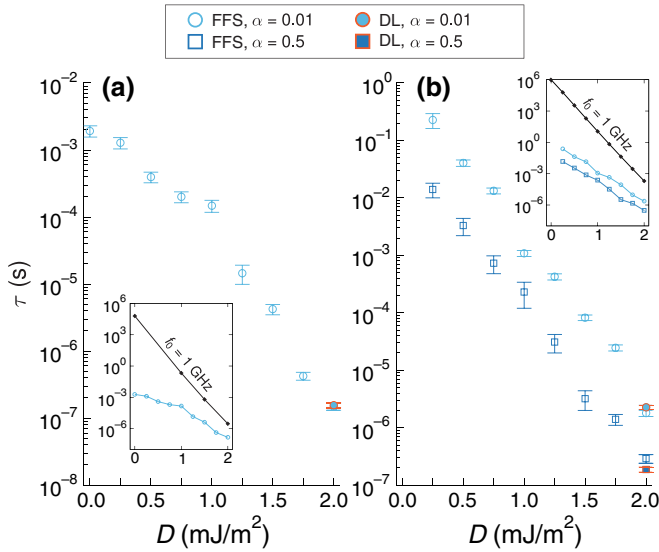
FIG. 7.   Average lifetime τ as a function of the DMI D at $T = 300$ K computed with FFS and direct Langevin (DL) dynamics simulations. (a) Lifetimes for $\alpha = 0.01$ with full dipole-dipole interactions. (b) Lifetimes for $\alpha = 0.01$ and $\alpha = 0.5$ with effective perpendicular anisotropy. The average lifetime computed from full Langevin dynamics simulations is given for all three cases at $D = 2$ mJ/m^2. The insets give a comparison of the FFS data with the constant $f_0 = 1$ GHz approximation and the energy barriers respectively computed in Refs. [5] and [43].

the rate is given by [32]

$$\sigma_k = k_{AB}\sqrt{\frac{\mathcal{V}}{N_0}}, \tag{12}$$

and is thus assumed to arise only from the trial runs. As anticipated from previous work, the lifetime appears to decrease with increasing DMI, which can be attributed to the linear decrease in the energy barrier with D that is directly related to the variation in the domain-wall energy (per unit surface area), $\sigma_w = 4\sqrt{\mathcal{A}K_u} - \pi D$. The striking result here however is the magnitude of τ, which varies from a few milliseconds at $D = 0$ to a few tenths of a microsecond at $D = 2$ mJ/m^2. These values are in stark contrast with the τ predicted by taking $f_0 = 1$ GHz with the energy barriers computed elsewhere [5], as shown in the inset of Fig. 7(a). This discrepancy stems from a strong entropic contribution to the prefactor [43], which results in a slower decrease of the overall lifetime as the barrier is reduced. In the present example, the constant f_0 approximation predicts a decrease by 10 orders of magnitude in τ as D is varied from 0 to 2 mJ/m^2, whereas the FFS results indicate a change of only 4 orders of magnitude over the same range. As we have shown elsewhere [43], a phenomenon of entropy-enthalpy compensation underpins this behavior, and the present example serves to highlight the importance of quantifying the Arrhenius prefactor

in magnetic nanostructures. Additionally, the lifetimes in Fig. 7(a) seem to display two regimes with two different slopes on the logarithmic scale. Since the internal energy barrier varies linearly with D [5], this behavior should stem from the prefactor, and may hint at complex interactions between the fluctuations and the wall under DMI and DDI. However, we note that these apparent two regimes could also be a numerical artifact resulting from an insufficient sampling in the A basin, since only $N_0 = 50$ initial trajectories are sampled in this case.

In Fig. 7(b), we present the lifetimes calculated with the effective anisotropy approximation for the underdamped ($\alpha = 0.01$) and overdamped ($\alpha = 0.5$) limits. The uncertainties in the lifetime are determined from Eq. (12) for $\alpha = 0.01$, whereas for $\alpha = 0.5$, they are obtained from several distinct FFS runs. The latter yields a larger error, because Eq. (12) neglects the statistical error that may stem from an incomplete sampling in the A basin, and treats the trial runs as the only source of error. In the underdamped case, we observe that the overall lifetimes are 2 orders of magnitude greater than those shown in Fig. 7(a). This is primarily due to the difference in energy barriers when the full dipolar interactions are taken into account, which amounts to a reduction of the barrier by about $4k_B T$ when dipolar interactions are included [5,43]. As for the Arrhenius prefactor, we find that, under a full treatment of the DDI, it is lower than in the effective anisotropy treatment for large D, while it is larger for low D [43]. Once more, the inset in Fig. 7(b) shows a comparison of the lifetimes with those obtained from the energy barriers [43] and the assumption of a constant value of f_0 equal to 1 GHz. While this assumption predicts a variation of τ by 8 orders of magnitude when D varies from 0.25 to 2 mJ/m^2, FFS simulations yield a variation by only 5 orders of magnitude over the same range. In the overdamped limit, the lifetimes decrease with the same overall slope as in the underdamped case, but are an order of magnitude shorter. This results from fewer barrier recrossings as compared to the underdamped case, and more generally from smaller deviations from thermodynamic equilibrium during the transition [43].

A comparison to direct Langevin simulations is possible for the lowest barriers studied, i.e., at $D = 2$ mJ/m^2, where the overall lifetimes remain accessible to direct integration of Eq. (6) for the full thermally activated switching process. These data are also presented in Fig. 7, where good quantitative agreement with the FFS results can be seen. The statistics and averaged time traces from these direct Langevin simulations are presented in Fig. 8. For each case studied, we perform 100 simulations of successful switching events with mean lifetimes in the range of 10 ns to 220 μs. The mean values are determined from exponential fits to the probability density distributions of the lifetime shown in Figs. 8(a), 8(c), and 8(e), while the uncertainties are determined from the variance. The time series data
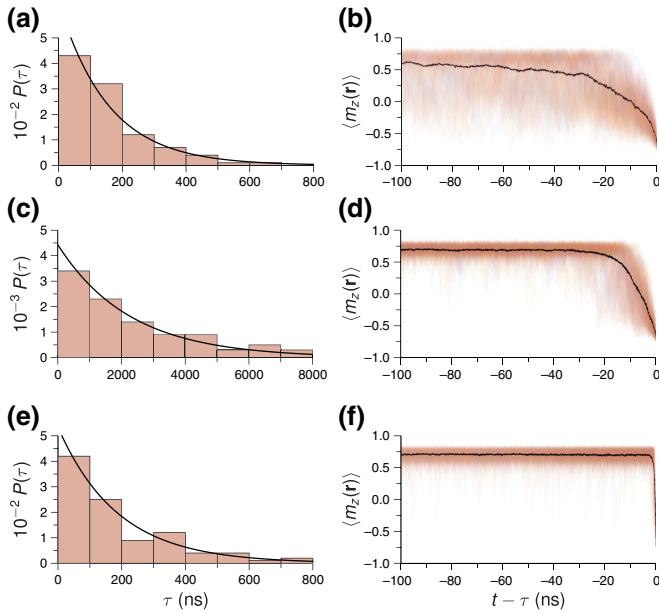
FIG. 8. Direct Langevin dynamics simulations of the dwell time τ for $D = 2$ mJ/m^2. The results correspond to (a),(b) $\alpha = 0.01$ with full dipolar interactions, (c),(d) $\alpha = 0.01$ with effective perpendicular anisotropy, and (e),(f) $\alpha = 0.5$ with effective perpendicular anisotropy. For each case, 100 simulations are performed with a successful switching event. (a),(c),(e) Probability distribution of the dwell time. The solid line represents a fit to an exponential function. (b),(d),(f) The m_z component of the magnetization as a function of time, where the curves are shifted along the time axis such that the first crossing of $-m_{z,0}$ occurs at $t = 0$. The colored curves represent the individual Langevin dynamics simulations, while the solid black line represents an average of these curves.

of m_z, shown for up to 100 ns before the full switching event, are presented in Figs. 8(b), 8(d), and 8(f). The underdamped limit is characterized by large fluctuations in the order parameter, where excursions to $m_z < 0$ can be seen frequently well before full reversal occurs. This behavior is most pronounced when full dipolar interactions are included [Fig. 8(b)] and is indicative of recrossing processes that ultimately lead to longer average dwell times in the A state. In contrast, the overdamped limit exhibits fewer excursions of this nature, where the time window in which large fluctuations occur are more localized to the switching event. This can also be seen in the solid black lines superimposed on the time series data, which represent averages over the 100 instances of the simulations and provide a measure of the reproducibility of the switching event. The averages for the underdamped cases exhibit a gradual decrease in $\langle m_z \rangle$ toward switching, while the variation is significantly sharper in the overdamped case.

In light of the previous observations, we show with black solid lines in Fig. 9 the cumulative conditional probabilities in FFS simulations normalized by P_B, $P(\lambda_i \mid \lambda_0)/P_B$, and averaged over all values of the DMI, as a
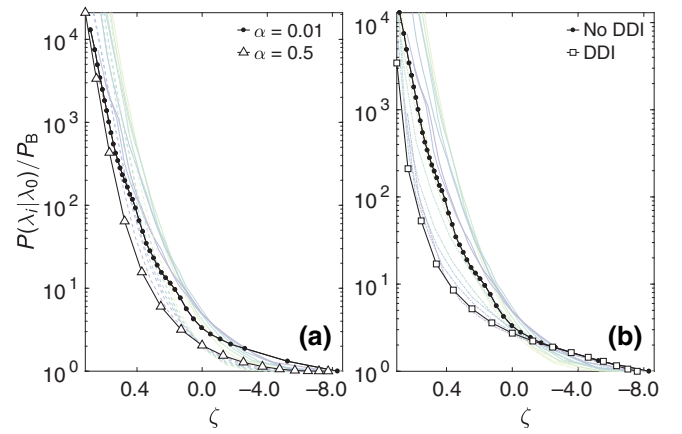

FIG. 9. Effects of (a) damping and (b) dipole-dipole interactions on the cumulative conditional probabilities normalized by P_B, $P(\lambda_i \mid \lambda_0)/P_B$. The transparent colored lines show the cumulative probabilities for all values of D as a function of the order parameter ζ, where the color of the line represents the value of D with the same colorscale as that of Fig. 6. In both graphs, the solid colored lines correspond to the underdamped case with effective anisotropy, while the dashed colored lines correspond to the other case. The black lines show the average cumulative conditional probabilities as a function of the average order parameter for each case.

function of the average order parameter ζ. The transparent colored lines correspond to the individual normalized cumulative probabilities for each value of D, where the color of the line corresponds to the value of the DMI according to the colorscale in Fig. 6.

In Fig. 9(a), we show the probabilities obtained with the effective anisotropy treatment, in the underdamped and overdamped regimes. As one might expect, the magnetization reverses more efficiently in the overdamped regime compared to the underdamped case, with an overall larger flux of forward trajectories along the order parameter and a faster saturation past the saddle point at $\zeta < 0$, which indicates fewer barrier recrossings. This is in line with the behavior of the magnetization in the direct Langevin simulations presented in Figs. 8(d) and 8(f).

In Fig. 9(b), we show the averaged cumulative conditional probabilities at a constant damping of $\alpha = 0.01$, with the effective anisotropy, and the full treatment of dipole-dipole interactions. In the portion of configuration space situated before the saddle point ($\zeta > 0$), the effect of DDI on the cumulative probabilities resembles that of the large Gilbert damping in Fig. 9(a), with a larger forward flux of trajectories than in the effective anisotropy treatment. However, the Langevin dynamics of the system under DDI, as shown in Fig. 8(b), is drastically different from the overdamped dynamics with effective anisotropy [Fig. 8(f)]. It seems that the DDI results in large fluctuations of the order parameter in the region of the A basin, which would explain the larger flux of forward trajectories

from λ_0 to the barrier top at $\lambda(\zeta = 0)$. Around that region, the amplitude of the fluctuations observed in Fig. 8(b) seems to decrease. This appears to coincide with a weaker flux of partial trajectories in Fig. 9(b), which now overlaps with the flux of trajectories corresponding to the effective anisotropy treatment.

IV. DISCUSSION AND CONCLUDING REMARKS

In this work, we have presented a detailed example of how rate constants for magnetic systems may be obtained by means of forward flux sampling simulations. The case detailed here concerns the mean waiting times between magnetization reversals as a function of DMI in a nanodisk with parameters similar to a free Co-Fe-B layer, as used in magnetoresistive random-access memories. In the large DMI case with the largest rate constant, FFS accurately reproduced the result of brute-force direct Langevin simulations, with and without a full treatment of dipole-dipole interactions.

When full DDIs are taken into account, and under a realistic Gilbert damping of $\alpha = 0.01$, the lifetime of the uniform state decreases with increasing DMI, and spans from a few milliseconds to tenths of a microsecond, while the stability factor, $\Delta = \beta_{300}\Delta E$, decreases from 32 to 8 [5]. In all the cases studied above, we find that the assumption $f_0 = 1$ GHz for the Arrhenius prefactor [5,7] is not justified, and does not hold. Indeed, the prefactor in this class of systems can take particularly large values, up to 10^{21} Hz, and varies drastically as a function of material parameters [43]. Such behavior stems from a mechanism of entropy-enthalpy compensation, also known as the Meyer-Neldel rule [47–50], and originates from the multiplicity of pathways to the barrier top. This phenomenon, ubiquitous across the natural sciences [50], concerns families of transitions among which a parameter such as, in the present case, the DMI, the applied magnetic field, or the effective anisotropy, is varied (see Ref. [43]), and should thus not be considered a special case limited to Co-Fe-B nanodisks, but a general result for domain-wall-mediated magnetization reversals. We note that this could even extend to other magnetic systems with large activation energies [47]. The present example serves to highlight the importance of quantifying the Arrhenius prefactor in magnetic nanostructures, and demonstrates how this can be achieved through forward flux sampling simulations.

It should be emphasized that the present study treats of mean waiting times between magnetization reversals, without concerning itself with the particular dynamics of the domain wall during said reversal. That is because the wall dynamics is not relevant for the considered transition rates, since the reversal is a rare event on the scale of the simulation, and the duration of the transition, i.e., the time it takes for the wall to sweep through the disk, is small compared to the mean waiting time between reversals.

Therefore, the particular dynamics of the transition is not considered in such a rare-event problem, for which the rate constant is assumed to be time invariant. Meanwhile, in Langevin simulations, the wall does not translate smoothly through the disk, but undergoes Brownian motion. During that time, the modes of deformation of the wall are excited by thermal fluctuations, and the size and shape of the wall vary a lot. The effect of the DMI on the dynamics of the current-driven magnetization reversal in a nanodisk has been studied in other works, such as Ref. [12], while its effect on the thermally activated reversal is characterized by the rate constant, which incorporates changes to the topology of the energy surface, and to the coupling to the magnon bath.

FFS can be used to compute time-invariant rate constants in systems in and out of equilibrium, that is, the method does not require detailed balance to hold. In addition to the rate constant and transition path ensemble, it can be used to obtain steady-state probability distributions as a function of one, or several, order parameter(s), and thus averages of experimental observables for comparison with experiments [33]. In all cases, FFS is most efficient when the choice of the order parameter is able to closely mimic the reaction coordinate.

[1] P. Hänggi, P. Talkner, and M. Borkovec, Reaction-rate theory: Fifty years after Kramers, Rev. Mod. Phys. **62**, 251 (1990).

[2] D. Weller and A. Moser, Thermal effect limits in ultrahigh-density magnetic recording, IEEE Trans. Magn. **35**, 4423 (1999).

[3] E. Chen, D. Apalkov, Z. Diao, A. Driskill-Smith, D. Druist, D. Lottis, V. Nikitin, X. Tang, S. Watts, and S. Wang *et al.*, Advances and future prospects of spin-transfer torque random access memory, IEEE Trans. Magn. **46**, 1873 (2010).

[4] M. Lederman, S. Schultz, and M. Ozaki, Measurement of the Dynamics of the Magnetization Reversal in Individual Single-Domain Ferromagnetic Particles, Phys. Rev. Lett. **73**, 1986 (1994).

[5] J. Sampaio, A. V. Khvalkovskiy, M. Kuteifan, M. Cubukcu, D. Apalkov, V. Lomakin, V. Cros, and N. Reyren, Disruptive effect of Dzyaloshinskii-Moriya interaction on the magnetic memory cell performance, Appl. Phys. Lett. **108**, 112403 (2016).

[6] D. Cortés-Ortuño, W. Wang, M. Beg, R. A. Pepper, M.-A. Bisotti, R. Carey, M. Vousden, T. Kluyver, O. Hovorka, and H. Fangohr, Thermal stability and topological protection of skyrmions in nanotracks, Sci. Rep. **7,** 4060 (2017).

[7] D. Gastaldo, N. Strelkov, L. D. Buda-Prejbeanu, B. Dieny, O. Boulle, P. Allia, and P. Tiberto, Impact of Dzyaloshinskii-Moriya interactions on the thermal stability factor of heavy metal/magnetic metal/oxide based nanopillars, J. Appl. Phys. **126,** 103905 (2019).

[8] S. Bhatti, R. Sbiaa, A. Hirohata, H. Ohno, S. Fukami, and S. N. Piramanayagam, Spintronics based random access memory: A review, Mater. Today **20,** 530 (2017).

[9] A. V. Khvalkovskiy, D. Apalkov, S. Watts, R. Chepulskii, R. S. Beach, A. Ong, X. Tang, A. Driskill-Smith, W. H. Butler, P. B. Visscher, D. Lottis, E. Chen, V. Nikitin, and M. Krounbi, Basic principles of STT-MRAM cell operation in memory arrays, J. Phys. D: Appl. Phys. **46,** 074001 (2013).

[10] G. D. Chaves-O'Flynn, G. Wolf, J. Z. Sun, and A. D. Kent, Thermal Stability of Magnetic States in Circular Thin-Film Nanomagnets with Large Perpendicular Magnetic Anisotropy, Phys. Rev. Appl. **4,** 024010 (2015).

[11] K. Munira and P. B. Visscher, Calculation of energy-barrier lowering by incoherent switching in spin-transfer torque magnetoresistive random-access memory, J. Appl. Phys. **117,** 17B710 (2015).

[12] P.-H. Jang, K. Song, S.-J. Lee, S.-W. Lee, and K.-J. Lee, Detrimental effect of interfacial Dzyaloshinskii-Moriya interaction on perpendicular spin-transfer-torque magnetic random access memory, Appl. Phys. Lett. **107,** 202401 (2015).

[13] T. Devolder, A. Le Goff, and V. Nikitin, Size dependence of nanosecond-scale spin-torque switching in perpendicularly magnetized tunnel junctions, Phys. Rev. B **93,** 224432 (2016).

[14] T. Devolder, J.-V. Kim, F. Garcia-Sanchez, J. Swerts, W. Kim, S. Couet, G. Kar, and A. Furnemont, Time-resolved spin-torque switching in MgO-based perpendicularly magnetized tunnel junctions, Phys. Rev. B **93,** 024420 (2016).

[15] M. Lavanant, P. Vallobra, S. Petit-Watelot, V. Lomakin, A. D. Kent, J. Sun, and S. Mangin, Asymmetric Magnetization Switching in Perpendicular Magnetic Tunnel Junctions: Role of the Synthetic Antiferromagnet's Fringe Field, Phys. Rev. Appl. **11,** 034058 (2019).

[16] I. Volvach, J. G. Alzate, Y. J. Chen, A. J. Smith, D. L. Kencke, and V. Lomakin, Thermal stability and magnetization switching in perpendicular magnetic tunnel junctions, Appl. Phys. Lett. **116,** 192408 (2020).

[17] S. Heinze, K. Von Bergmann, M. Menzel, J. Brede, A. Kubetzka, R. Wiesendanger, G. Bihlmayer, and S. Blügel, Spontaneous atomic-scale magnetic skyrmion lattice in two dimensions, Nat. Phys. **7,** 713 (2011).

[18] C. Moreau-Luchaire, C. Moutafis, N. Reyren, J. Sampaio, C. Vaz, N. Van Horne, K. Bouzehouane, K. Garcia, C. Deranlot, and P. Warnicke *et al.*, Additive interfacial chiral interaction in multilayers for stabilization of small individual skyrmions at room temperature, Nat. Nanotechnol. **11,** 444 (2016).

[19] M. Heide, G. Bihlmayer, and S. Blügel, Dzyaloshinskii-Moriya interaction accounting for the orientation of magnetic domains in ultrathin films: Fe/W(110), Phys. Rev. B **78,** 140403(R) (2008).

[20] J. Wild, T. N. G. Meier, S. Pöllath, M. Kronseder, A. Bauer, A. Chacon, M. Halder, M. Schowalter, A. Rosenauer, J. Zweck, J. Müller, A. Rosch, C. Pfleiderer, and C. H. Back, Entropy-limited topological protection of skyrmions, Sci. Adv. **3,** e1701704 (2017).

[21] P. F. Bessarab, G. P. Müller, I. S. Lobanov, F. N. Rybakov, N. S. Kiselev, H. Jónsson, V. M. Uzdin, S. Blügel, L. Bergqvist, and A. Delin, Lifetime of racetrack skyrmions, Sci. Rep. **8,** 3433 (2018).

[22] L. Desplat, D. Suess, J.-V. Kim, and R. L. Stamps, Thermal stability of metastable magnetic skyrmions: Entropic narrowing and significance of internal eigenmodes, Phys. Rev. B **98,** 134407 (2018).

[23] L. Desplat, J.-V. Kim, and R. L. Stamps, Paths to annihilation of first- and second-order (anti)skyrmions via (anti)meron nucleation on the frustrated square lattice, Phys. Rev. B **99,** 174409 (2019).

[24] S. von Malottki, P. F. Bessarab, S. Haldar, A. Delin, and S. Heinze, Skyrmion lifetime in ultrathin films, Phys. Rev. B **99,** 060409(R) (2019).

[25] L. Desplat, C. Vogler, J.-V. Kim, R. L. Stamps, and D. Suess, Path sampling for lifetimes of metastable magnetic skyrmions and direct comparison with Kramers' method, Phys. Rev. B **101,** 060403(R) (2020).

[26] H. Kramers, Brownian motion in a field of force and the diffusion model of chemical reactions, Physica **7,** 284 (1940).

[27] J. Langer, Statistical theory of the decay of metastable states, Ann. Phys. **54,** 258 (1969).

[28] F. Garcia-Sanchez, P. Borys, A. Vansteenkiste, J.-V. Kim, and R. L. Stamps, Nonreciprocal spin-wave channeling along textures driven by the Dzyaloshinskii-Moriya interaction, Phys. Rev. B **89,** 224408 (2014).

[29] F. Garcia-Sanchez, P. Borys, R. Soucaille, J.-P. Adam, R. L. Stamps, and J.-V. Kim, Narrow Magnonic Waveguides Based on Domain Walls, Phys. Rev. Lett. **114,** 247206 (2015).

[30] P. Borys, F. García-Sánchez, J.-V. Kim, and R. L. Stamps, Spin-wave eigenmodes of dzyaloshinskii domain walls, Adv. Electron. Mater. **2,** 1500202 (2015).

[31] R. J. Allen, P. B. Warren, and P. Rein ten Wolde, Sampling Rare Switching Events in Biochemical Networks, Phys. Rev. Lett. **94,** 2340 (2005).

[32] R. J. Allen, D. Frenkel, and P. R. ten Wolde, Simulating rare events in equilibrium or nonequilibrium stochastic systems, J. Chem. Phys. **124,** 024102 (2006).

[33] R. J. Allen, C. Valeriani, and P. Rein ten Wolde, Forward flux sampling for rare event simulations, J. Phys.: Condens. Matter **21,** 463102 (2009).

[34] E. E. Borrero and F. A. Escobedo, Simulating the kinetics and thermodynamics of transitions via forward flux/umbrella sampling, J. Phys. Chem. B **113,** 6434 (2009).

[35] C. Vogler, F. Bruckner, B. Bergmair, T. Huber, D. Suess, and C. Dellago, Simulating rare switching events of magnetic nanostructures with forward flux sampling, Phys. Rev. B **88,** 134409 (2013).

[36] C. Vogler, F. Bruckner, D. Suess, and C. Dellago, Calculating thermal stability and attempt frequency of advanced recording structures without free parameters, J. Appl. Phys. **117,** 163907 (2015).

[37] A. N. Bogdanov and U. K. Rößler, Chiral Symmetry Breaking in Magnetic Thin Films and Multilayers, Phys. Rev. Lett. **87,** 037203 (2001).

[38] A. Vansteenkiste, J. Leliaert, M. Dvornik, M. Helsen, F. García-Sánchez, and B. Van Waeyenberge, The design and verification of MuMax3, AIP Adv. **4,** 107133 (2014).

[39] W. F. Brown, Thermal fluctuations of a single-domain particle, Phys. Rev. **130,** 1677 (1963).

[40] J. L. García-Palacios and F. Lázaro, Langevin-dynamics study of the dynamical properties of small magnetic particles, Phys. Rev. B **58,** 14937 (1998).

[41] J. Leliaert, J. Mulkers, J. De Clercq, A. Coene, M. Dvornik, and B. Van Waeyenberge, Adaptively time stepping the stochastic landau-lifshitz-Gilbert equation at nonzero temperature: Implementation and validation in MuMax 3, AIP Adv. **7,** 125010 (2017).

[42] S. Rohart and A. Thiaville, Skyrmion confinement in ultrathin film nanostructures in the presence of Dzyaloshinskii-Moriya interaction, Phys. Rev. B **88,** 184422 (2013).

[43] L. Desplat and J.-V. Kim, Entropy-Reduced Retention Times in Magnetic Memory Elements: A Case of the Meyer-Neldel Compensation Rule, Phys. Rev. Lett. **125,** 107201 (2020).

[44] C. Bilzer, T. Devolder, J.-V. Kim, G. Counil, C. Chappert, S. Cardoso, and P. P. Freitas, Study of the dynamic magnetic properties of soft CoFeB films, J. Appl. Phys. **100,** 053903 (2006).

[45] D.-X. Chen, J. A. Brug, and R. B. Goldfarb, Demagnetizing factors for cylinders, IEEE Trans. Magn. **27,** 3601 (1991).

[46] P. F. Bessarab, V. M. Uzdin, and H. Jonsson, Method for finding mechanism and activation energy of magnetic transitions, applied to skyrmions and antivortex annihilation, Comput. Phys. Commun. **196,** 335 (2015).

[47] E. Peacock-López and H. Suhl, Compensation effect in thermally activated processes, Phys. Rev. B **26,** 3774 (1982).

[48] A. Yelon and B. Movaghar, Microscopic Explanation of the Compensation (Meyer-Neldel) Rule, Phys. Rev. Lett. **65,** 618 (1990).

[49] A. Yelon, B. Movaghar, and H. M. Branz, Origin and consequences of the compensation (meyer-neldel) law, Phys. Rev. B **46,** 12244 (1992).

[50] A. Yelon, B. Movaghar, and R. Crandall, Multi-excitation entropy: Its role in thermodynamics and kinetics, Rep. Prog. Phys. **69,** 1145 (2006).